










# Optical frequency combs in dispersion-controlled doubly resonant second-harmonic generation

IOLANDA RICCIARDI,<sup>1,2,\*</sup>  PASQUALE MADDALONI,<sup>1,2</sup>   
PAOLO DE NATALE,<sup>3</sup>  MIRO ERKINTALO,<sup>4</sup>  TOBIAS HANSSON,<sup>5</sup>  
ADY ARIE,<sup>6</sup>  STEFAN WABNITZ,<sup>1,7</sup>  AND MAURIZIO DE ROSA<sup>1,2</sup> 

<sup>1</sup>CNR-INO, Istituto Nazionale di Ottica, Via Campi Flegrei 34, I-80078 Pozzuoli (NA), Italy

<sup>2</sup>INFN, Istituto Nazionale di Fisica Nucleare, Sez. di Napoli, Complesso Universitario di M.S. Angelo, Via Cintia, Napoli I-80126, Italy

<sup>3</sup>CNR-INO, Istituto Nazionale di Ottica, largo E. Fermi 6, I-50125 Firenze, Italy

<sup>4</sup>The Dodd-Walls Centre for Photonic and Quantum Technologies, Department of Physics, The University of Auckland, Auckland 1142, New Zealand

<sup>5</sup>Department of Physics, Chemistry and Biology, Linköping University, SE-581 83 Linköping, Sweden

<sup>6</sup>School of Electrical Engineering, Iby and Aladar Fleischman Faculty of Engineering, Tel-Aviv University, Tel-Aviv 69978, Israel

<sup>7</sup>Dipartimento di Ingegneria dell'Informazione, Elettronica e Telecomunicazioni, Sapienza Università di Roma, Via Eudossiana 18, I-00184 Roma, Italy

\*iolanda.ricciardi@ino.cnr.it

**Abstract:** We report on the experimental realization and a systematic study of optical frequency comb generation in doubly resonant intracavity second harmonic generation (SHG). The efficiency of intracavity nonlinear processes usually benefits from the increasing number of resonating fields. Yet, achieving the simultaneous resonance of different fields may be technically complicated, all the more when a phase matching condition must be fulfilled as well. In our cavity we can separately control the resonance condition for the fundamental and its second harmonic, by simultaneously acting on an intracavity dispersive element and on a piezo-mounted cavity mirror, without affecting the quasi-phase matching condition. In addition, by finely adjusting the laser-to-cavity detuning, we are able to observe steady comb emission across the whole resonance profile, revealing the multiplicity of comb structures, and the substantial role of thermal effects on their dynamics. Lastly, we report the results of numerical simulations of comb dynamics, which include photothermal effects, finding a good agreement with the experimental observations. Our system provides a framework for exploring the richness of comb dynamics in doubly resonant SHG systems, assisting the design of chip-scale quadratic comb generators.

© 2022 Optica Publishing Group under the terms of the [Optica Open Access Publishing Agreement](#)

## 1. Introduction

In the last few years, optical frequency comb generation by purely quadratic processes has been demonstrated both in continuously pumped singly resonant intracavity second harmonic generation (SHG) [1] and optical parametric oscillators (OPOs) [2,3], highlighting peculiar advantages, such as the simultaneous emission of octave-distant combs and the capability to directly access elusive spectral regions. More recently, optical frequency combs have been observed in millimeter-size whispering gallery mode resonators, where the primary process of SHG is naturally phase matched and both the fundamental and second harmonic fields can simultaneously resonate [4,5]. The appearance of comb emission in quadratically nonlinear resonators can be explained as the result of cascaded  $\chi^{(2)}$ : $\chi^{(2)}$  processes. For instance, in the resonator studied here, the second harmonic field generated by the primary nonlinear process may act, above a given power threshold, as the pump for secondary parametric oscillations,

generating a first couple of side modes around the pump frequency. After that, other secondary  $\chi^{(2)}$  processes generate new frequencies around the pump and its second harmonic, eventually leading to comb spectra. More generally, the formation of  $\chi^{(2)}$  frequency combs can be described in the framework of a modulation instability [6]. Experimental observations of quadratic combs stimulated theoretical modeling of their dynamics, unveiling a rich nonlinear behavior, including the emergence of stable temporal patterns (pulse trains) and corresponding optical frequency combs [7–9]. Localized states and cavity solitons have been predicted and theoretically analyzed in the absence of temporal walk-off [10–12]. Experimentally, comb generation in cavity-enhanced SHG was first realised in a bulk free-space resonator where only the fundamental pump was resonant [1]. Such free-space resonators offer means to controllably explore the comb generation process by permitting straightforward stabilization of the cavity and independent tuning of various parameters. Simultaneous resonance of the fundamental and harmonic fields is ideally fulfilled in monolithic devices where birefringent phase matching is achieved and total internal reflection is adopted, though in practice a trade-off between resonance condition and optimal phase matching is required [13,14]. The presence of multi-layered Bragg mirrors or alternative quasi-phase matching schemes necessitate a stronger compensation of the intracavity dispersion. Different solutions have been proposed, yet rare experimental realizations have been reported, where simultaneous resonance was achieved by acting on the temperature of the nonlinear crystal, at the price of a non-optimal phase matching, or by misaligning the crystal itself [15,16]. As a matter of fact, these technical complications essentially limited the use of doubly resonant resonators to monolithic configurations, with birefringent phase matching.

Here, we demonstrate frequency comb generation in a bulk, free-space, doubly resonant intracavity SHG, where several critical system parameters can be individually adjusted, thus permitting a thorough experimental analysis of comb formation. In particular, the resonance condition can be separately controlled for the fundamental frequency (FF) and its second harmonic (SH), without affecting the SHG phase-matching condition, which is independently regulated by changing the temperature of the nonlinear crystal. Moreover, thanks to a stable and versatile cavity locking scheme, we are able to explore a wide range of frequency detunings across a cavity resonance, where different comb spectra can be observed. Our experiments provide significant insights on comb formation in doubly resonant SHG systems, and, despite being performed in a bulk cavity, could inform the design and operation of whispering gallery mode-based or chip-scale quadratic comb generators, enabled by recent advances in the fabrication of chip-scale LiNbO<sub>3</sub> photonic devices [17–22].

## 2. Experimental setup

A scheme of the experimental setup is shown in Fig. 1(a). The second harmonic generator is based on a lithium niobate nonlinear crystal placed in a traveling-wave optical cavity, pumped by a cw narrow-linewidth Nd:YAG laser, emitting 0.5 W at 1064.45 nm. The cavity consists of two spherical (100 mm of radius of curvature) and two plane mirrors in a bow-tie configuration and is resonant for frequencies around both the fundamental pump and the second harmonic. The pump beam enters the cavity through a partially reflective flat coupling mirror ( $R = 98\%$  @ 1064 nm,  $R = 92.5\%$  @ 532 nm), while the remaining mirrors are high reflection coated at both 1064 and 532 nm ( $R > 99.9\%$  @ 1064/532 nm for the two curved mirrors,  $R > 99.7\%$  @ 1064/532 nm for the remaining plane mirror). The high reflective flat mirror is mounted on a piezoelectric actuator (PZT) for cavity length control. The measured cavity free spectral range and linewidth (FWHM) are 504 MHz and 3.0 MHz, respectively, resulting in a finesse of 168. The nonlinear crystal, placed between the two curved mirrors, is a 15-mm-long, 5%-MgO-doped lithium niobate sample, periodically poled with a 1°-slant grating period of  $\Lambda = 6.92 \mu\text{m}$ . Input and output crystal facets are polished at a 1°-wedge angle in order to prevent back reflected radiation from resonating inside the cavity. The crystal temperature is actively stabilized by a

Peltier element driven by an electronic servo control. Phase matching of the SHG process for the fundamental wavelength occurs at a crystal temperature  $T_0 = 63.4^\circ\text{C}$ . In addition, the cavity baseplate is thermally stabilized within few hundredths of Celsius degree, through a second temperature servo control, ensuring long term stable operation.

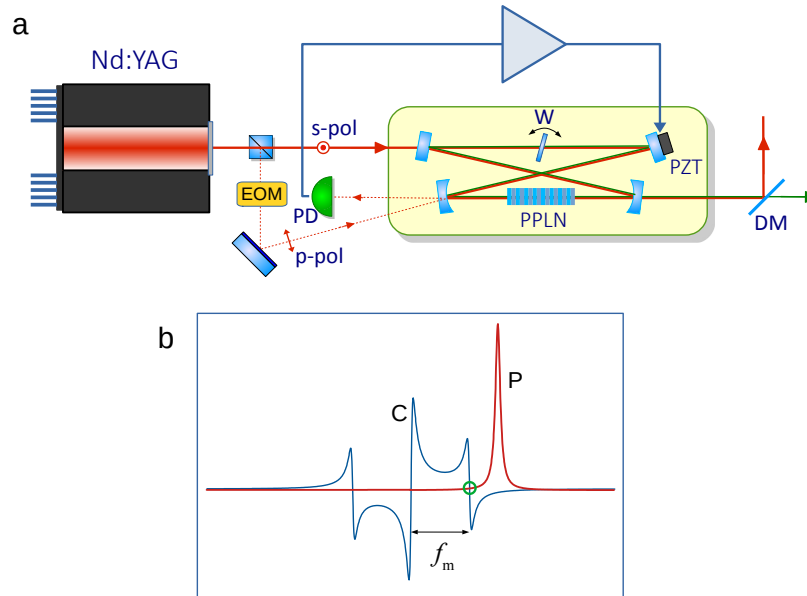


**Fig. 1.** (a) Experimental scheme of the doubly resonant SHG cavity. Periodically poled lithium niobate (PPLN), fused silica window (W), electro-optic modulator (EOM), piezoelectric actuator (PZT), dichroic mirror (DM), photodiode (PD). (b) Schematic view of the signals used for cavity offset locking, as a function of the cavity length. P is a resonance for the primary beam. C is the Pound–Drever–Hall signal around a resonance of the counterpropagating auxiliary beam. The green circle marks the locking point.

Unlike the case for birefringent phase matching, in our quasi-phase matched crystal the FF and SH fields experience different refractive index values, and consequently different cavity optical paths. In order to compensate the effect of dispersion at the fundamental and harmonic frequency, we inserted in the cavity an angle-adjustable, 3-mm-thick silica window. A rotation of the window simultaneously changes the round-trip phase delay to a different extent for each field, and, as a consequence, the resonance condition. By successively acting on the cavity length, through the piezo-mounted cavity mirror, we always re-establish the resonance of the pump field, while the SH can be set in any state between resonant or anti-resonant. We notice that the presence of the window slightly modifies the cavity dispersion to all orders, however with negligible effect on the field dynamics. More important, the quasi-phase matching condition is not influenced by the presence of the window. Thermal stabilization of the entire cavity allows to maintain the resonance condition for several hours. The cavity is locked to the pump laser frequency by acting on the PZT, via the Pound–Dever–Hall offset locking technique [23]. To this end, while the cavity is pumped by a high-power, vertically polarized pump beam (primary beam), an orthogonally polarized, low power auxiliary beam is phase modulated through an electro-optic modulator and sent to the cavity in the opposite direction of the nonlinear generation process. The use of orthogonally polarized light prevents detrimental interactions between backward and forward beams inside the cavity. In general, because of the crystal birefringence, the two beams resonate for two different cavity lengths; however, by properly choosing the modulation frequency  $f_m$ , it is

possible to make one sideband of the auxiliary beam resonate in the vicinity of the primary beam. The cavity is thus locked in correspondence to that sideband, and, by varying the modulation frequency, it is possible to change the relative position of the primary beam frequency and the corresponding nearest cavity resonance (see Fig. 1(b)). Fundamental light leaving the cavity is separated from second harmonic light by a dichroic mirror and sent to an optical spectrum analyzer with a spectral range from 600-1700 nm, unable to provide a direct spectral image of SH combs. Evidence of combs around the SH is given by monitoring the SH output light by a 1-GHz-FSR confocal Fabry–Pérot cavity, where all the detected modes are mapped within one FSR of the analysis cavity [1].

### 3. Results

When the FF and SH are simultaneously on resonance, the typical power threshold for the onset of the internally pumped OPO (i.e. the generation of the first couple of sidebands) is as low as 5 mW. Panels (a)-(e) in Fig. 2 show examples of comb spectra observed when the cavity is offset locked to the laser and cavity-to-laser detuning is slowly changed (over several minutes) by sweeping the modulation frequency  $f_m$ . Figure 2(f) displays the cavity transmission profile of the pump frequency for increasing (red curve) and decreasing (blue curve) detunings. The silica window was adjusted to make the FF and SH simultaneously resonate. The laser power impinging on the cavity was 300 mW. Similar sequences of comb structures have been observed for different pump powers, and the comb structures are reproducible and stable over several tens of minutes.

Slow scans around a resonance reveal clear signatures of photothermal effects, as shown in the power transmission profile of Fig. 2(f). Photothermal effect is due to light that is absorbed when passing through the crystal and the mirrors' reflective layers, and converted into heat [24]. The resulting increase of the local temperature of the crystal produces, via thermal expansion and the thermo-optic effect, a change of the cavity optical path proportional to the intracavity optical power. Here, we can reasonably assume that the crystal is the dominant source of thermal effects. When the red-detuned resonance approaches the laser, the increasing intracavity power leads to a corresponding increase of the cavity optical path, via the photothermal effect. As a result, the observed resonance profile is stretched towards higher relative frequencies. On the contrary, when the resonance approaches the laser from the blue detuned side, for the same effect, the resonance is pulled toward the laser, resulting in a hysteretic behaviour associated to thermal induced bistability, which is absent in fast scans, where different stationary states are reached depending on the direction the resonance is approached. Transitions between different emission regimes appear in the experimental power profile as steep power changes, followed by flat sections. We guess that a passive thermal locking mechanism [24] opposes to the frequency scan driven by our active locking, producing a sharp transition every time the scan pulling overcomes the thermal locking strength. This effect is more evident where thermal locking is stronger, i.e., near the top of the resonance, such as for the large flat segment around point c in Fig. 2(f). However, despite the long duration of each detuning sweep, the sequence of comb spectra is largely reproduced from one scan to the other.

We notice that, while the change in the optical path due to thermal expansion is the same for both fields and polarizations, the contribution of the opto-thermal effect depends on polarization and frequency of the intracavity fields. Therefore, Fig. 2(f) actually shows the differential shift between the primary and auxiliary beam. Similarly, the second harmonic field experiences a slightly different resonance shift with respect to the fundamental field.

For increasingly negative detunings, the comb width becomes more and more narrow, while a pair of side modes appears  $\sim 16$  nm from the FF, and initially coexists with a thin central comb [Fig. 3(a) and inset]. As the detuning gets even larger, only the side modes survive [Fig. 3(b)], until they finally disappear. We spatially separated the pump mode and the two sidebands using a

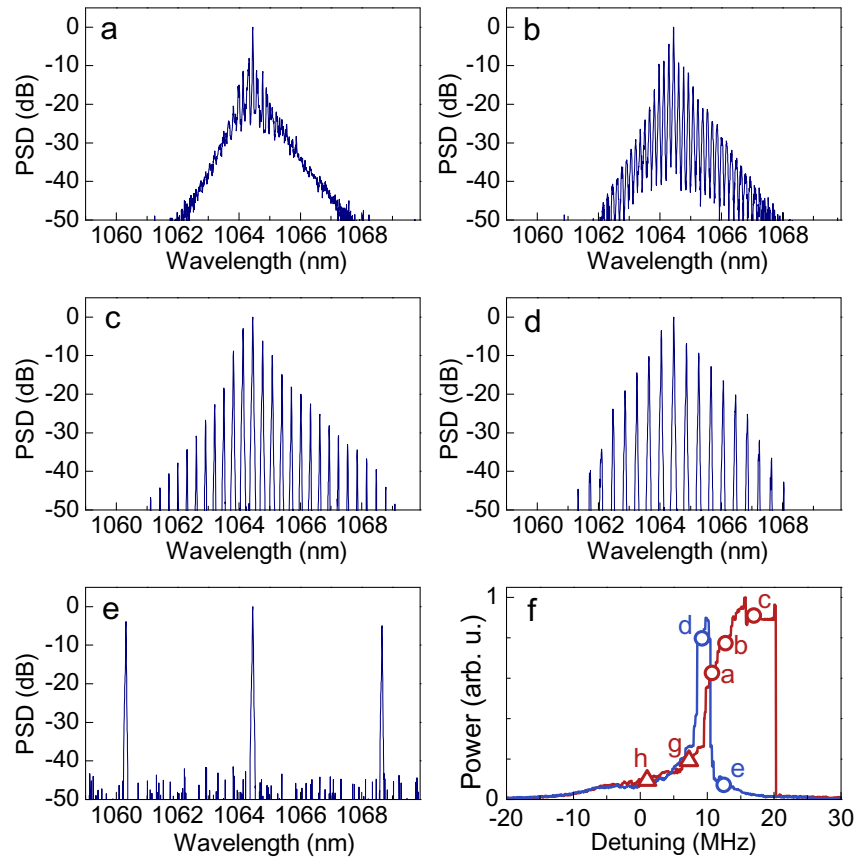


**Fig. 2.** (a)-(e) Experimental comb spectra around the FF with an input power of 300 mW for different frequency detunings, under condition of simultaneous resonance of FF and SH beams. (f) Cavity transmission profiles of the FF for increasing (red curve) and decreasing (blue curve) detunings. The labeled circles correspond to spectra in (a)-(e). Zero in the frequency axis marks the ‘cold’ resonance position, measured with very low pump power. Triangles correspond to spectra shown in Fig. 3.

diffraction grating, and analyzed the transverse structure of each mode by a CCD camera. The side modes had the transverse power distribution of a first order Hermite-Gauss mode  $TEM_{10}$ , as shown in the inset of Fig. 3(b), while the pump and SH modes were carried by the fundamental transverse Gaussian beam  $TEM_{00}$ . This result can be understood as follows. The parametric mode pair that eventually prevails in an OPO is the one with the lowest oscillation threshold, which depends inversely on nonlinear coupling strength and linearly on mode detunings [25]. In fact, the nonlinear coupling strength between three interacting modes is proportional to the overlap integral of their transverse mode functions [26,27], which is different from zero depending on the symmetry of the product of the involved mode functions. If the OPO is pumped by a  $TEM_{00}$  beam (we recall that, in our case, the SH field is the internal pump of the cascaded OPO), the maximum overlap integral occurs when both signal and idler oscillate in a  $TEM_{00}$  mode. However, a nonzero overlap integral occurs also for parametric oscillations with both signal and idler in a  $TEM_{10}$  mode (or  $TEM_{01}$ ). On the other hand, detuning between signal or idler and the respective closest cavity mode is minimized for a couple of *symmetric* modes, i.e., equidistant from the pump frequency. For null or small detunings of the fundamental frequency

$\omega$ , parametric oscillations occur for longitudinal modes close to the central frequency, from which they are nearly equidistant. As the cavity is negatively detuned, closer longitudinal resonances become less and less equidistant, leading to larger signal/idler detunings. On the contrary, a couple of higher-order transverse modes, which initially are overly *asymmetric*, can be found in a more *symmetric* configuration, eventually attaining the lowest oscillation threshold and prevailing on longitudinal modes. It is worth noting that also the two side modes of Fig. 2(e) can be easily separated by the grating. We thus verified that they oscillate in a TEM<sub>00</sub> mode, as expected. The high-order modes are steadily visible for a pump power as low as 50 mW, with a power per mode of the order of several mW, measured out of the coupling mirror.

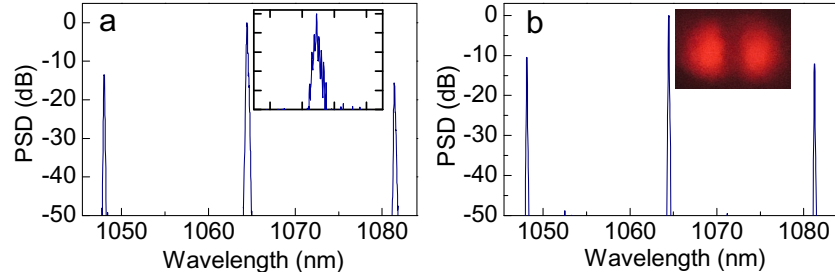


**Fig. 3.** Spectra corresponding to triangle marks of Fig. 2. (a) For a detuning around 7 MHz (point g in Fig. 2(f)) a new pair of side modes appears  $\sim 16$  nm from the FF, coexisting with a narrow central comb. In the inset, an enlarged view of the central comb (axis scales, 1 nm/div, 10 dB/div). (b) For lower detunings, (point h in Fig. 2(f)) around 0 MHz only the side modes survive, at the expense of the central comb, which vanishes. The inset is an image of the transverse pattern of the distant side modes.

Doubly resonant, phase-matched SHG dynamics can be well described by two coupled mean-field equations for the fundamental and second harmonic field,  $A$  and  $B$ , respectively, which read [9]

$$t_R \frac{\partial A}{\partial t} = \left[ -\alpha_1 - i\delta_1 - i \frac{k_1 L}{2} \frac{\partial^2}{\partial \tau^2} \right] A + i\kappa L B A^* + \sqrt{\theta_1} A_{\text{in}}, \quad (1)$$

$$t_R \frac{\partial B}{\partial t} = \left[ -\alpha_2 - i\delta_2 - \Delta k' L \frac{\partial}{\partial \tau} - i \frac{k_2 L}{2} \frac{\partial^2}{\partial \tau^2} \right] B + i\kappa L A^2, \quad (2)$$

where  $t_R$  is the cavity round-trip time;  $t$  is a slow time variable that describes field evolution on the time scale of the cavity photon lifetime;  $\tau$  is a fast time variable that describes the temporal profiles of cavity fields;  $\alpha_j$  represent total cavity losses for the corresponding field (hereafter, subscripts 1 and 2 denote fields  $A$  and  $B$ , respectively);  $\delta_j \simeq (\omega_{c,j} - \omega_j)t_R$  is the detuning between the optical field  $\omega_j$  and the closest cavity resonance  $\omega_{c,j}$ , which includes the effect of the photothermal dynamics, as explained below;  $\Delta k'$  is the walk-off parameter;  $k_j$  is the group velocity dispersion coefficient;  $\kappa$  is the nonlinear coupling constant;  $L$  is the length of the nonlinear crystal;  $A_{\text{in}}$  is the external coherent driving field at the FF; and  $\theta_1$  is the power transmission coefficient of the coupling mirror. We numerically integrated the mean-field equations, including the photothermal effect, in order to better simulate the experimental conditions. Photothermal dynamics strongly depends on the particular resonator configuration [24,28]. In a simplified model, the time scale of thermal dynamics is governed by the thermal diffusion time  $\tau_{\text{th}}$  across the beam radius,  $\tau_{\text{th}} = \rho C r^2 / \kappa$ , where  $\rho$ ,  $C$ ,  $\kappa$  are density, specific heat and thermal conductivity of the material (i.e., the nonlinear crystal), and  $r$  is the mean beam waist of the optical mode inside the crystal. In our case,  $\rho = 4.65 \times 10^3$  kg/m<sup>3</sup>,  $C = 648$  J/kg K,  $\kappa = 4.4$  W/m K,  $r = 5 \times 10^{-5}$  m, and we estimate  $\tau_{\text{th}} \sim 1.7$  ms, which is about four orders of magnitude slower than the cavity photon lifetime ( $\sim 100$  ns), which governs the dynamics of the cavity fields. Consequently, cavity

fields reach a steady state on a much faster time scale than thermal induced dynamics. We can thus include the thermal effect as an extra detuning term, in addition to the “cold” detuning  $\delta_{j,0}$ , due to the change of the cavity geometric length through the PZT, by substituting in Eqs. (1)–(2)  $\delta_j = \delta_{j,0} + j\delta_{th}$ , where  $\delta_{th} = \xi P$  is proportional to the intracavity optical power, averaged over thousands of round trip times.  $\xi$  represents the thermal sensitivity parameter, obtained by the ratio between the heat-detuning conversion coefficient and the thermal relaxation coefficient of the resonator [29].

In our simulations, we assumed the second harmonic process to be phase matched, and swept the detuning in discrete steps from negative to positive values and back, around the resonance for both the FF and SH. For each detuning step the numerical integration is performed over 10 000 round-trip times, for a total of  $\sim 10^7$  round-trips for a complete scan. Fig. 4(a)–(e) shows examples of calculated FF spectra for different frequency detunings, indicated by labeled circles on the cavity transmission profiles in panel (f). In the same panel, the calculated transmission curve obtained by not including the thermal effect is shown for comparison. The sequence of comb spectra as a function of  $\Delta = \delta_1/\alpha_1$  is essentially similar to that calculated in the absence of thermal effects, except for part of the resonance which is inaccessible due to thermal instability. Calculated spectra show an overall good agreement with the measured ones, except for a difference in the intermodal spacing of some spectra. Spectra on the left side of the resonance [Fig. 4(a)–(c)] are common to both the scan directions, which correspond to similar power levels [Fig. 4(f)], as they do not depend on the sweeping direction. However, they are partially accessible in the experiment due to the observed competition of parametric oscillation in high-order modes, which are not included in the simulations. We finally notice that the calculated power transmission curves, as shown in Fig. 4(f), display a rather regular variation, aside for the noise, whereas the experimental profiles, as in Fig. 2(f), appear as steep power changes, followed by flat sections. In this regard, we notice that numerical simulation does not include the dynamics induced by the presence of the active locking, as well as by the passive thermal locking mechanism, which we conjecture are responsible for the observed irregular power profiles in Fig. 2(f).

By rotating the intracavity window, we modified the resonance condition, so that when the pump is resonant the SH field is strongly detuned from resonance. Panels (a)–(e) in Fig. 5 show examples of observed spectra. In this case, the threshold for comb emission is higher than in the resonant case, and combs are restricted to a smaller detuning interval, which can be reached only when the resonance is approached from negative detunings. [Fig. 5(f)]. When the resonance is swept from the blue side, thermal pulling skips the detuning range where combs occur. Also in this case, for a narrow detuning range, a parametric oscillation in a pair of distant modes appears for the maximum available power, shown in Fig. 5(e). However, in this case the oscillation occurs in TEM<sub>00</sub> modes. As for the theoretical model, it is worth noting that Eqs. (1) and (2) are valid in the approximation of small detunings, when compared to the cavity FSR, and do not apply to the last experiment. A more general numerical approach may be adopted, at the cost of an increased computation time, based on an infinite-dimensional map in the time domain, which involves propagation equations for the two fields, coupled with appropriate boundary conditions, linking the fields between successive roundtrips [8].

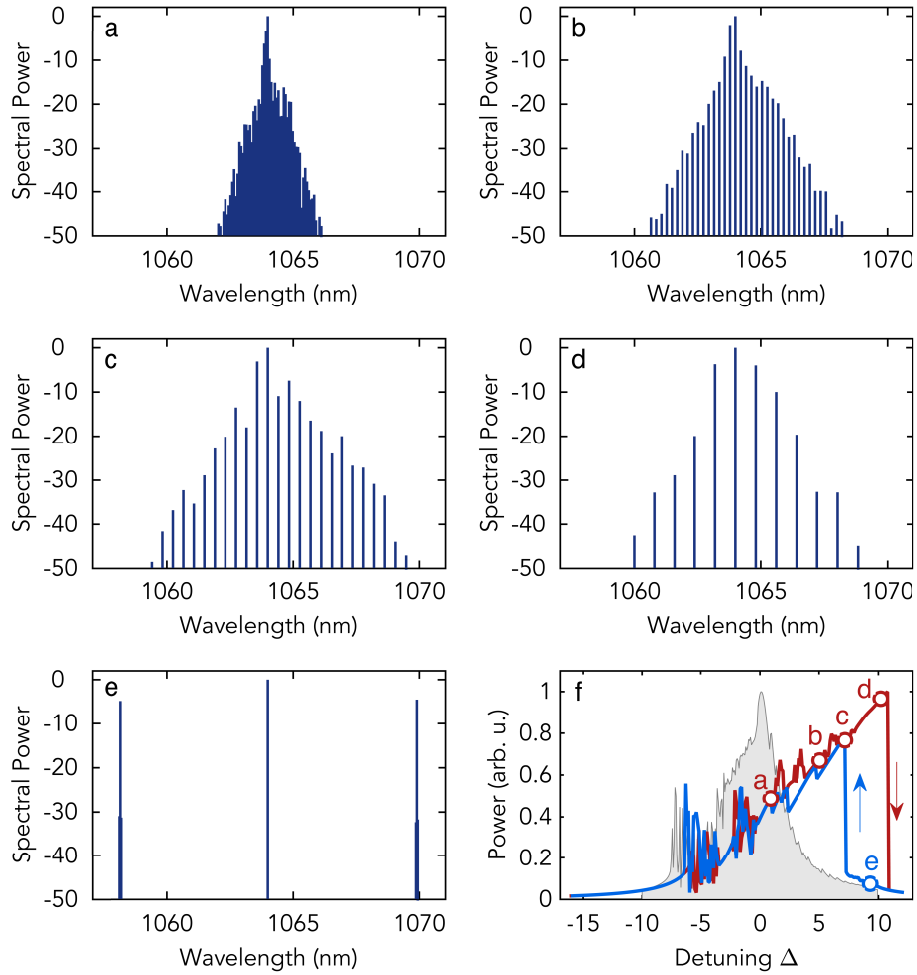


**Fig. 4.** Numerical simulation of comb formation in the presence of thermal effects. (a)-(e) Comb spectra for different detunings. (f) Cavity power profiles as a function of the normalized detuning  $\Delta = \delta_1/\alpha_1$ , for forward (red curve) and backward (blue curve) sweep. Circles indicate the panel of the corresponding spectrum. The shaded profile was obtained from numerical solution without thermal effect. Parameters used for the simulation are  $\alpha_1 = 0.02$ ,  $\alpha_2 = 0.0575$ ,  $L = 15$  mm,  $\Delta k' = 792$  ps/m,  $k_1 = 0.234$  ps<sup>2</sup>/m,  $k_2 = 0.714$  ps<sup>2</sup>/m,  $\theta_1 = 0.02$ ,  $A_{in} = \sqrt{300}$  mW,  $\xi = -0.08$  W<sup>-1</sup>.



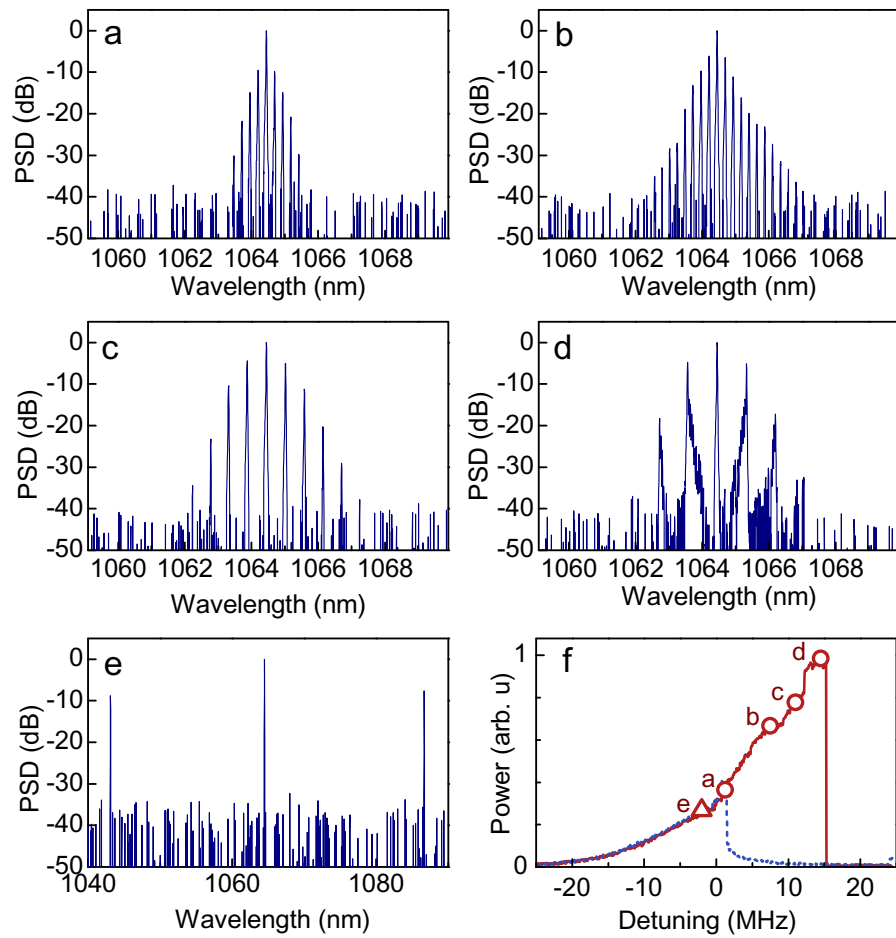


**Fig. 5.** (a)-(e) Experimental spectra around the FF with an input power of 250 mW for five different frequency detunings, in condition of resonant FF and antiresonant SH. (f) Cavity transmission profiles of the FF for increasing (red curve) and decreasing (blue curve) detunings. The labeled circles correspond to spectra in (a)-(d). The triangle corresponds to the spectrum in (e) consisting of two distant side modes.

#### 4. Conclusions

In conclusion, we presented a versatile doubly resonant cavity SHG system for the generation of quadratic combs. The system permits to change continuously from simultaneous resonance for FF and SH to resonant FF and fully non-resonant SH. In addition, an offset locking scheme allows to finely adjust and maintain the laser-to-cavity detuning over a range of several cavity linewidths. Thanks to the wide locking range, we were able to explore and control the whole landscape of emission regimes, which includes an unexpected transition from comb emission in longitudinal modes to parametric oscillation in a pair of high-order modes. The onset of the latter oscillation, which in our case prevents further comb emission, can be managed by a proper design of the resonator geometry and dispersion. The power threshold for comb onset is substantially reduced, compared to a singly resonant bulk cavity, and is similar to that observed in monolithic whispering-gallery-mode  $\chi^{(2)}$  nonlinear resonators [5]. The locking scheme can be further improved, in order to reduce the influence of thermal effects [30], and allow a systematic study of the comb coherence. Preliminary measurement, limited to combs spaced by one FSR, does not indicate a high degree of coherence, in agreement with the prediction of numerical calculations. On the contrary, widely spaced combs, corresponding to Turing pattern in the temporal domain, are expected to exhibit a higher coherence. Progress in realization of small footprint LiNbO<sub>3</sub> photonic devices already enables the realization of high-quality microresonators, with alternative phase matching schemes, where nonlinear conversion processes can be efficiently performed [17–22,31–34]. Our system provides a flexible testbed for investigating comb dynamics over a large set of physical parameters.

**Funding.** PON Ricerca e Innovazione 2014/2020 FESR/FSC (ARS01\_00734, QUANCOM); Agenzia Spaziale Italiana (NIHL); Horizon 2020 Framework Programme (820419, FET Flagship on Quantum Technologies, Qombs Project); Ministero degli Affari Esteri e della Cooperazione Internazionale (NOICE Joint Laboratory).

**Disclosures.** The authors declare no conflicts of interest.

**Data availability.** Data underlying the results presented in this paper are available from the authors upon reasonable request.

#### References

1. I. Ricciardi, S. Mosca, M. Parisi, P. Maddaloni, L. Santamaria, P. De Natale, and M. De Rosa, "Frequency comb generation in quadratic nonlinear media," *Phys. Rev. A* **91**(6), 063839 (2015).
2. V. Ulvila, C. R. Phillips, L. L. Halonen, and M. Vainio, "Frequency comb generation by a continuous-wave-pumped optical parametric oscillator based on cascading quadratic nonlinearities," *Opt. Lett.* **38**(21), 4281–4284 (2013).
3. S. Mosca, M. Parisi, I. Ricciardi, F. Leo, T. Hansson, M. Erkintalo, P. Maddaloni, P. De Natale, S. Wabnitz, and M. De Rosa, "Modulation instability induced frequency comb generation in a continuously pumped optical parametric oscillator," *Phys. Rev. Lett.* **121**(9), 093903 (2018).
4. I. Hendry, L. S. Trainor, Y. Xu, S. Coen, S. G. Murdoch, H. G. L. Schwefel, and M. Erkintalo, "Experimental observation of internally pumped parametric oscillation and quadratic comb generation in a  $\chi^{(2)}$  whispering-gallery-mode microresonator," *Opt. Lett.* **45**(5), 1204–1207 (2020).
5. J. Szabados, D. N. Puzyrev, Y. Minet, L. Reis, K. Buse, A. Villosio, D. V. Skryabin, and I. Breunig, "Frequency comb generation via cascaded second-order nonlinearities in microresonators," *Phys. Rev. Lett.* **124**(20), 203902 (2020).
6. I. Ricciardi, S. Mosca, M. Parisi, F. Leo, T. Hansson, M. Erkintalo, P. Maddaloni, P. D. Natale, S. Wabnitz, and M. De Rosa, "Optical frequency combs in quadratically nonlinear resonators," *Micromachines* **11**(2), 230 (2020).
7. S. Mosca, I. Ricciardi, M. Parisi, P. Maddaloni, L. Santamaria, P. De Natale, and M. De Rosa, "Direct generation of optical frequency combs in  $\chi^{(2)}$  nonlinear cavities," *Nanophotonics* **5**(2), 316–331 (2016).
8. F. Leo, T. Hansson, I. Ricciardi, M. De Rosa, S. Coen, S. Wabnitz, and M. Erkintalo, "Walk-off-induced modulation instability, temporal pattern formation, and frequency comb generation in cavity-enhanced second-harmonic generation," *Phys. Rev. Lett.* **116**(3), 033901 (2016).
9. F. Leo, T. Hansson, I. Ricciardi, M. De Rosa, S. Coen, S. Wabnitz, and M. Erkintalo, "Frequency-comb formation in doubly resonant second-harmonic generation," *Phys. Rev. A* **93**(4), 043831 (2016).
10. T. Hansson, P. Parra-Rivas, M. Bernard, F. Leo, L. Gelens, and S. Wabnitz, "Quadratic soliton combs in doubly resonant second-harmonic generation," *Opt. Lett.* **43**(24), 6033–6036 (2018).
11. A. Villosio and D. V. Skryabin, "Soliton and quasi-soliton frequency combs due to second harmonic generation in microresonators," *Opt. Express* **27**(5), 7098–7107 (2019).
12. P. Parra-Rivas, C. M. Arabi, and F. Leo, "Dark quadratic localized states and collapsed snaking in doubly resonant dispersive cavity-enhanced second-harmonic generation," *Phys. Rev. A* **104**(6), 063502 (2021).

13. A. Sizmann, R. J. Horowicz, G. Wagner, and G. Leuchs, "Observation of amplitude squeezing of the up-converted mode in second harmonic generation," *Opt. Commun.* **80**(2), 138–142 (1990).
14. S. Schiller and R. L. Byer, "Quadruply resonant optical parametric oscillation in a monolithic total-internal-reflection resonator," *J. Opt. Soc. Am. B* **10**(9), 1696–1707 (1993).
15. S. Pereira, M. Xiao, H. J. Kimble, and J. L. Hall, "Generation of squeezed light by intracavity frequency doubling," *Phys. Rev. A* **38**(9), 4931–4934 (1988).
16. C. Zimmermann, R. Kallenbach, T. W. Hänsch, and J. Sandberg, "Doubly-resonant second-harmonic generation in  $\beta$ -barium-borate," *Opt. Commun.* **71**(3-4), 229–234 (1989).
17. G. Lin, J. U. Fürst, D. V. Strekalov, and N. Yu, "Wide-range cyclic phase matching and second harmonic generation in whispering gallery resonators," *Appl. Phys. Lett.* **103**(18), 181107 (2013).
18. J. Lin, Y. Xu, J. Ni, M. Wang, Z. Fang, L. Qiao, W. Fang, and Y. Cheng, "Phase-matched second-harmonic generation in an on-chip LiNbO<sub>3</sub> microresonator," *Phys. Rev. Appl.* **6**(1), 014002 (2016).
19. R. Wolf, I. Breunig, H. Zappe, and K. Buse, "Cascaded second-order optical nonlinearities in on-chip micro rings," *Opt. Express* **25**(24), 29927–29933 (2017).
20. S. Liu, Z. Fang, X. Ye, Y. Cheng, Y. Zheng, and X. Chen, "Effective four-wave mixing in the lithium niobate on insulator microdisk by cascading quadratic processes," *Opt. Lett.* **44**(6), 1456–1459 (2019).
21. J. Lu, M. Li, C.-L. Zou, A. Al Sayem, and H. X. Tang, "Toward 1% single-photon anharmonicity with periodically poled lithium niobate microring resonators," *Optica* **7**(12), 1654–1659 (2020).
22. J. Lu, A. A. Sayem, Z. Gong, J. B. Surya, C.-L. Zou, and H. X. Tang, "Ultralow-threshold thin-film lithium niobate optical parametric oscillator," *Optica* **8**(4), 539–544 (2021).
23. R. W. P. Drever, J. L. Hall, F. V. Kowalski, J. Hough, G. M. Ford, A. J. Munley, and H. Ward, "Laser phase and frequency stabilization using an optical resonator," *Appl. Phys. B* **31**(2), 97–105 (1983).
24. T. Carmon, L. Yang, and K. J. Vahala, "Dynamical thermal behavior and thermal self-stability of microcavities," *Opt. Express* **12**(20), 4742–4750 (2004).
25. T. Debuisschert, A. Sizmann, E. Giacobino, and C. Fabre, "Type-II continuous wave optical parametric oscillators: oscillation and frequency-tuning characteristics," *J. Opt. Soc. Am. B* **10**(9), 1668–1680 (1993).
26. C. Schwob, P.-F. Cohadon, C. Fabre, M. Marte, H. Ritsch, A. Gatti, and L. Lugiato, "Transverse effects and mode couplings in OPOS," *Appl. Phys. B* **66**(6), 685–699 (1998).
27. G. B. Alves, R. F. Barros, D. S. Tasca, C. E. R. Souza, and A. Z. Khoury, "Conditions for optical parametric oscillation with a structured light pump," *Phys. Rev. A* **98**(6), 063825 (2018).
28. M. De Rosa, L. Conti, M. Cerdonio, M. Pinard, and F. Marin, "Experimental measurement of the dynamic photothermal effect in Fabry-Perot cavities for gravitational wave detectors," *Phys. Rev. Lett.* **89**(23), 237402 (2002).
29. A. Leshem, Z. Qi, T. F. Carruthers, C. R. Menyuk, and O. Gat, "Thermal instabilities, frequency-comb formation, and temporal oscillations in Kerr microresonators," *Phys. Rev. A* **103**(1), 013512 (2021).
30. H. Zhou, Y. Geng, W. Cui, S.-W. Huang, Q. Zhou, K. Qiu, and C. W. Wong, "Soliton bursts and deterministic dissipative Kerr soliton generation in auxiliary-assisted microcavities," *Light: Sci. Appl.* **8**(1), 50 (2019).
31. M. Zhang, C. Wang, R. Cheng, A. Shams-Ansari, and M. Lončar, "Monolithic ultra-high-Q lithium niobate microring resonator," *Optica* **4**(12), 1536–1537 (2017).
32. R. Wu, J. Zhang, N. Yao, W. Fang, L. Qiao, Z. Chai, J. Lin, and Y. Cheng, "Lithium niobate micro-disk resonators of quality factors above  $10^7$ ," *Opt. Lett.* **43**(17), 4116–4119 (2018).
33. J. Lin, N. Yao, Z. Hao, J. Zhang, W. Mao, M. Wang, W. Chu, R. Wu, Z. Fang, L. Qiao, W. Fang, F. Bo, and Y. Cheng, "Broadband quasi-phase-matched harmonic generation in an on-chip monocrystalline lithium niobate microdisk resonator," *Phys. Rev. Lett.* **122**(17), 173903 (2019).
34. J. Lu, J. B. Surya, X. Liu, A. W. Bruch, Z. Gong, Y. Xu, and H. X. Tang, "Periodically poled thin-film lithium niobate microring resonators with a second-harmonic generation efficiency of 250, 000%/W," *Optica* **6**(12), 1455–1460 (2019).